Fundamental Duty Modulation of Dual-Active-Bridge Converter for Wide-Range Operation

Wooin Choi, *Student Member, IEEE*, Kyung-Min Rho, and Bo-Hyung Cho, *Fellow, IEEE*

***Abstract*—This paper proposed a modulation scheme for the dual-active-bridge (DAB) converter to reduce rms current in wide-range operating conditions. The operating principle of the proposed fundamental duty modulation (FDM) is formulated based on the fundamental component analysis of the DAB converter. By modulating the PWM signals in the fundamental component domain, the optimal operation is implemented with a simple controller structure not requiring an operating mode classification, offline calculation, or current information. Operating characteristics including rms current level and ZVS characteristics are analyzed to compare loss breakdowns of the proposed scheme to those of recent related works. The proposed FDM achieves high efficiency under wide operation conditions due to reduced conduction level and wide ZVS range. Experimental results are obtained under various voltage gain and load conditions to confirm the operation of the proposed modulation scheme. A thorough experimental comparison with other sophisticated modulation schemes has verified the efficiency improvement of FDM.**

***Index Terms*—Dual-active bridge (DAB), fundamental component analysis (FCA), fundamental duty modulation (FDM), isolated bidirectional dc–dc converter, modulation scheme.**

I. Introduction

SINCE its introduction [1], the dual-active bridge (DAB) shown in Fig. 1 has been an appealing topology for bidirectional power conversion applications with galvanic isolation [2]–[8]. The DAB converter utilizes the leakage inductance of the high-frequency transformer as a power transfer element, therefore increasing the power density. The converter shows high efficiency by achieving zero-voltage switching (ZVS) without the need for additional resonant components. Moreover, the symmetric circuit topology on the primary and secondary sides of the transformer can allow fast and smooth bidirectional power flow control by shifting the phase between the sides for positive to negative.

A large portion of the DAB literature focuses on developing a modulation scheme for the converter in a wide-range operation [10]–[22]. As depicted in Fig. 1, excluding a frequency variation, the DAB converter has three degrees of freedom d_1, d_2, ϕ in modulating PWM gating signals of both sides of the bridges. Phase ϕ is the phase difference between the bridges. Duty ratios d_1, d_2 are controlled by shifting the phase between PWM signals of the legs within a bridge. Various efforts have been made to find an optimal set of d_1, d_2, ϕ for improved efficiency over an entire-load range and wide-voltage range.

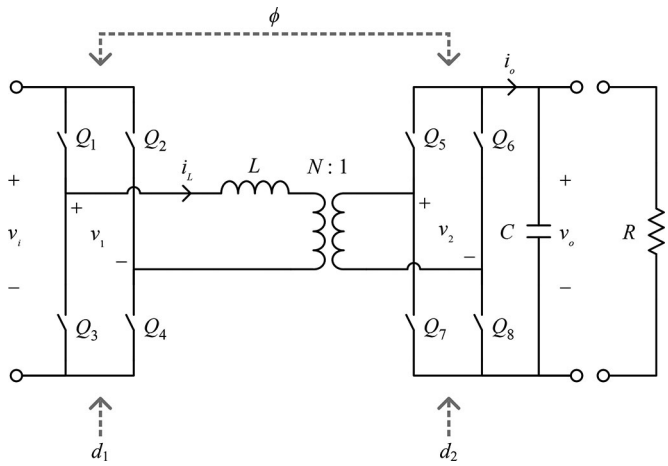

Fig. 1. Circuit diagram of the DAB converter.

Phase shift modulation (PSM) which is the most commonly used modulation scheme regulates the converter by modulating the phase ϕ [10]. PSM scheme is simple to implement and easy to control since it has one degree of freedom of modulation. However, the main disadvantage of the conventional PSM which has been tackled by many researcher is the poor efficiency at light load and non-unity voltage gain condition. This is due to the full-duty feature of PSM which inherently induces a large circulating current compared to the average output current especially at light load. Furthermore, ZVS ranges of the secondary-side switches are limited as load decreases, which results in an increased switching loss and noise.

To overcome aforementioned limitations of PSM, alternative modulation methods have been proposed to find an optimal solution with increased degrees of freedom utilizing d_1, d_2, ϕ. Based on an intuitive approach, there have been suggested modulation schemes, such as the triangular modulation (TRM) [11]–[14] or the dual phase shift [15], [16], to reduce conduction and switching losses. However, the operating range and the optimality of these works are limited. On the other hand, optimal schemes based on thorough and complex investigation using time-domain analysis have been employed in [21]–[23]. A critical disadvantage of these optimal modulation techniques

Manuscript received April 6, 2015; revised June 24, 2015; accepted August 12, 2015. Date of publication August 28, 2015; date of current version January 7, 2016. Recommended for publication by Associate Editor R. Ayyanar.

W. Choi and B.-H. Cho are with the Department of Electrical and Computer Engineering, Seoul National University, Seoul 110-744, Korea (e-mail: wooin.choi@gmail.com; bhcho@snu.ac.kr).

K.-M. Rho is with the Department of Mathematical Sciences, Seoul National University, Seoul 110-744, Korea (e-mail: leftwing@snu.ac.kr).

Color versions of one or more of the figures in this paper are available online at http://ieeexplore.ieee.org.

Digital Object Identifier 10.1109/TPEL.2015.2474135

is the complexity from which heavy computation and/or mode classification with respect to output power level is inevitable. Moreover, the methods in [21] and [22] require the large amount of online and offline calculations. The principles of the series of these studies are lying on a tradeoff between the complexity and the optimality of the modulation scheme.

On the other hand, there have been several proposals to find an optimal modulation scheme for an improved efficiency based on the fundamental component analysis (FCA) [24], [25]. Using the FCA, the DAB converter can be analyzed by approximating the ac signals (such as inductor current and transformer voltages) to their fundamental components. The benefits of the FCA over the time-domain analysis are: 1) equations of active and reactive power are expressed in simple analytic forms; 2) the analytic equations are applicable to the entire operating ranges; and 3) the inductor current dynamics are included in the model.

In this paper, fundamental duty modulation (FDM) is proposed that utilizes the optimal solution of minimization of current conduction obtained from the FCA model. While the conventional modulation techniques directly compute the modulation signals, (d_1, d_2, ϕ), the modulation principle of FDM is to compute an optimal set of the modulation signals expressed in a simple form in the fundamental component domain $(d_{1,\alpha}, d_{1,\beta}, d_{2,\alpha})$. Therefore, with a simple controller structure, FDM does not require an operating mode classification, offline calculation, or current information.

However, the limitation of an FCA model is that 1) the model cannot reflect switching instants which determines switching characteristics, and 2) the model is established on approximation neglecting higher order Fourier coefficients. For these reason, in this paper, operating characteristics of FDM including rms current level and ZVS characteristics are analyzed by transforming the FDM modulation scheme in time domain. Based on the analysis, the power loss model is derived to compare the performance of FDM to those of recent related works [23], [24]. The proposed solution results in reduced conduction loss and improved efficiency for wide operating region regardless of voltage gain or power level.

This paper is organized as follows. Section II introduces the modeling strategy of the DAB using the FCA. In Section III, an optimal solution and modulation scheme of FDM are formulated based on the FCA model. A detailed implementation procedure of the proposed scheme is given with an eased calculation burden. In Section IV, qualitative and quantitative features of FDM were examined and compared to recent related works. Loss model is established to estimate the improvement on efficiency under various voltage gain and output power conditions. Experimental results for verification of the proposed modulation scheme are delivered in Section V.

II. DAB Modeling Using an FCA

The proposed FDM achieves an optimal modulation of the DAB converter utilizing the model derived using the FCA. The steady-state characteristics of the DAB converter with respect to fundamental component can be expressed in a simple and universal form.

A circuit diagram of the DAB converter is shown in Fig. 1 where v_i and v_o are the input and output voltages, respectively, v_1 and v_2 are the voltages induced at each side of the transformer, i_L and i_o are the inductor current and the output current, respectively, L is the leakage inductance of the transformer, and C is the output capacitance. It is assumed that leakage inductances are reflected to the primary side, and the magnetizing inductance is infinite. The turn ratio of the transformer is hereafter assumed to be 1 without the loss of generality.

A. Modeling Principles

Electric values of the DAB converter, such as i_L, v_1, and v_2 in Fig. 1, have a zero average dc value. Hence, using the conventional averaging technique, these states are averaged out to zero. Instead, these states can be decomposed to their fundamental components using a Fourier transformation. A periodic signal $x(t)$ can be represented as

$$x(t) \approx \frac{x_0}{2} + x_\alpha \sin\omega t + x_\beta \cos\omega t \tag{1}$$

where x_α and x_β are computed by

$$\begin{aligned} x_\alpha &= \frac{2}{T_s}\int_0^{T_s} (x(t)\sin\omega t)\, dt \\ x_\beta &= \frac{2}{T_s}\int_0^{T_s} (x(t)\cos\omega t)\, dt. \end{aligned} \tag{2}$$

Accordingly, the inductor current and the primary- and secondary-side voltages are decomposed, respectively, as

$$i_L(t) \approx 0 + i_\alpha \sin\omega t + i_\beta \cos\omega t \tag{3}$$

and

$$\begin{aligned} v_1(t) &= v_i(t)\cdot v_{1,n}(t) \approx v_i(t)\cdot(d_{1,\alpha}\sin\omega t + d_{1,\beta}\cos\omega t) \\ v_2(t) &= v_o(t)\cdot v_{2,n}(t) \approx v_o(t)\cdot(d_{2,\alpha}\sin\omega t + d_{2,\beta}\cos\omega t) \end{aligned} \tag{4}$$

where ω is given as 2π times f_s, the switching frequency, $v_{1,n}$ and $v_{2,n}$ are normalized voltage of v_1 and v_2, respectively, and $d_{1,\alpha}$, $d_{1,\beta}$, $d_{2,\alpha}$, and $d_{2,\beta}$ are modulation signals in the FCA domain which are defined below. As in (4), v_1 and v_2 are determined by the modulation signals. The time-domain signals, duty ratios d_1 and d_2, and phase ϕ are generated by a combination of PWM signals of the transistors as depicted in Fig. 2. Every switch pair in a leg (e.g., Q_1 and Q_3) works complementarily. d_1 and d_2 are synthesized by shifting the phase between switching legs (Q_1 and Q_2 for d_1, and Q_5 and Q_6 for d_2), basically set to 0.5 for PSM. The phase difference between the primary- and the secondary-side switches (Q_1 and Q_5) determines ϕ.

The Fourier coefficients, $(d_{1,\alpha}, d_{1,\beta}, d_{2,\alpha}$, and $d_{2\beta})$, are expressed in time-domain values (d_1, d_2 and ϕ) using the relation in (2) as

$$\begin{aligned} d_{1,\alpha} &= \frac{4}{\pi}\sin\pi d_1 \cos 2\pi\phi \\ d_{1,\beta} &= \frac{4}{\pi}\sin\pi d_1 \sin 2\pi\phi \\ d_{2,\alpha} &= \frac{4}{\pi}\sin\pi d_2 \\ d_{2,\beta} &= 0. \end{aligned} \tag{5}$$

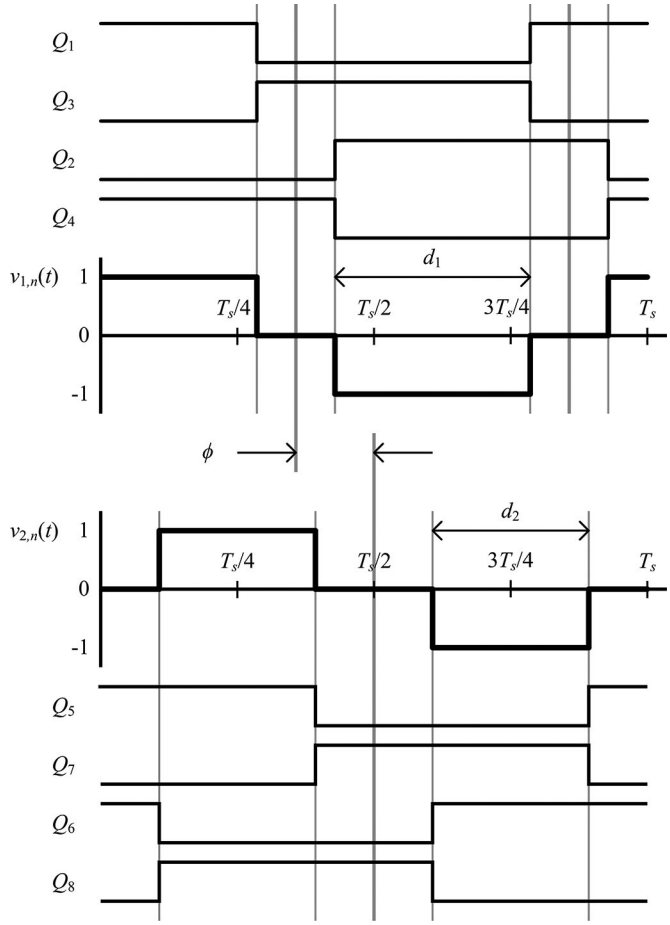

Fig. 2. Normalized transformer voltages according to PWM gating signals of Q_1–Q_8.

Note that $d_{2,\beta}$ is zero since the transformation interval in (2) is set with respect to $v_{2,n}(t)$. The modulation variable set d_1, d_2, ϕ in the time domain is now translated into $d_{1,\alpha}$, $d_{1,\beta}$, $d_{2,\alpha}$ in the FCA domain.

B. Dynamic Equations

Neglecting the series resistances, dynamic equation of the inductor current of the DAB converter is expressed as

$$L\frac{di_L}{dt} = v_1 - v_2. \tag{6}$$

After substituting (3) and (4) into (6), the α- and β-domain equations are obtained, respectively, as

$$\begin{aligned} L\frac{di_\alpha}{dt} - \omega L i_\beta &= d_{1,\alpha}v_i - d_{2,\alpha}v_o \\ L\frac{di_\beta}{dt} + \omega L i_\alpha &= d_{1,\beta}v_i. \end{aligned} \tag{7}$$

However, i_o, the output-side current is computed as the zeroth Fourier component of the product of i_L and d_2 as

$$i_o = \frac{1}{2}\left(d_{2,\alpha}i_\alpha + d_{2,\beta}i_\beta\right) = \frac{1}{2}d_{2,\alpha}i_\alpha. \tag{8}$$

TABLE I
CONVERTER SPECIFICATIONS: SIMPLIFIED MODEL

Parameter		Value
Input voltage	V_i	200 V
Output voltage	V_o	100 to 200 V
Turn ratio	N	1
Switching frequency	f_s	50 kHz
Inductance	L	100 μH
Voltage gain	M	0.5 to 1.0
Maximum output power	$P_{\max}$	500 to 1000 W

The capacitor dynamic equation is given from (8) as

$$C\frac{dv_o}{dt} = \frac{1}{2}d_{2,\alpha}i_\alpha - \frac{v_o}{R}. \tag{9}$$

C. Steady-State Characteristics

Steady-state values can be calculated by equating the dynamic equations (7) and (8) to zero, respectively. Capitalized letters refer to steady-state values and I_o, I_α, and I_β are obtained as

$$\begin{aligned} I_o &= \frac{1}{2}D_{2,\alpha}I_\alpha \\ I_\alpha &= \frac{1}{X_L}D_{1,\beta}V_i, I_\beta = -\frac{1}{X_L}\left(D_{1,\alpha}V_i - D_{2,\alpha}V_o\right) \end{aligned} \tag{10}$$

where X_L is ωL. The transferred power of the converter is, then, given as

$$P_o = V_o \cdot I_o = \frac{V_i \cdot V_o}{2X_L}D_{2,\alpha}D_{1,\beta}. \tag{11}$$

The absolute value of the fundamental component inductor current is

$$\|I_L\| = \sqrt{I_\alpha^2 + I_\beta^2} = \frac{V_i}{X_L}\sqrt{D_{1,\beta}^2 + \left(D_{1,\alpha} - M \cdot D_{2,\alpha}\right)^2} \tag{12}$$

where M is the voltage gain V_o/V_i. Using the traditional time-domain analysis, the steady-state characteristics should be calculated regarding the switching patterns. As in a previous study [22], the switching patterns of the DAB converter are classified into up to 12 cases. However, the universal operating characteristics in (11) and (12) can be applicable to the entire operating region [1].

For specifications listed in Table I, operating characteristics of the DAB converter using the FCA are calculated from (11) and (12), and those of the time-domain analysis are obtained from a numerical method. In Fig. 3, the output powers and the rms currents using the FCA and the time-domain analysis are shown as black and gray lines, respectively. For ease in depicting the difference between the time-domain analysis and the FCA, steady-state investigation is conducted for $d_2 = 0.5$, and various voltage gains, where M for $N \neq 1$ is defined as

$$M = \frac{NV_o}{V_i}. \tag{13}$$

Although the steady-state analysis of the FCA generally coincides with the time-domain results, there is an error since the

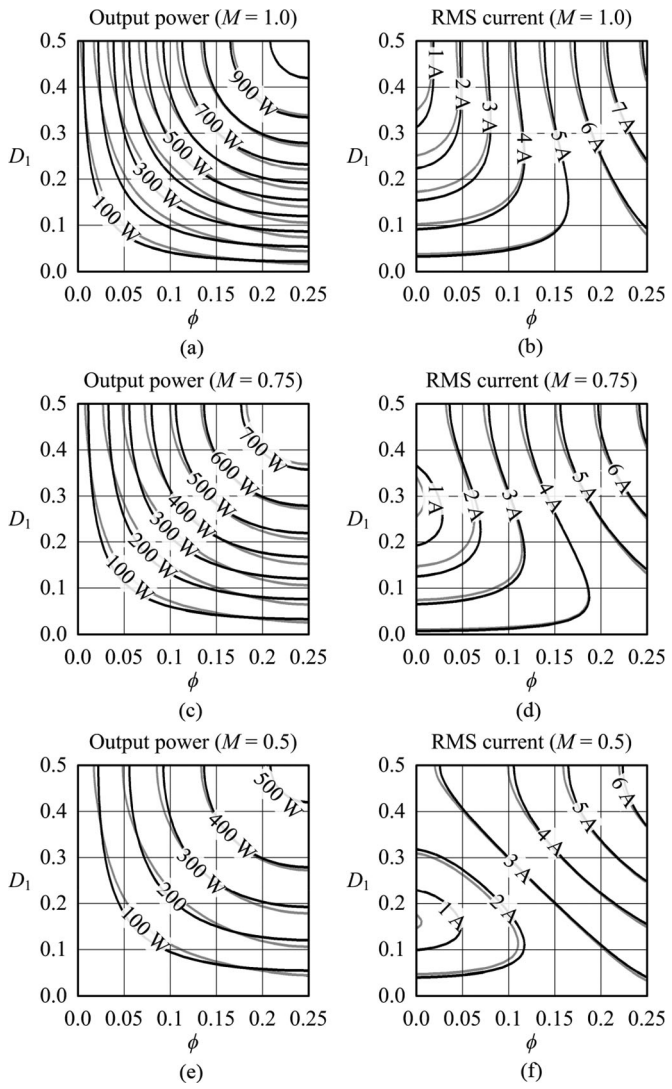

Fig. 3. Output power and rms current calculation based on the FCA (black) and the time-domain analysis (gray): (a) and (b) for $M = 1.0$, (c) and (d) for $M = 0.75$, and (e) and (f) for $M = 0.5$.

FCA is based on the first-order approximation. Errors in the rms currents calculation grow as ϕ decreases. Especially, the error becomes comparably larger for low ϕ and low M in Fig. 3(f). As will be treated, this inaccuracy of the rms current at light load affects the operating characteristics of the proposed modulation strategy.

III. Fundamental Duty Modulation

Modulation principle of FDM is formulated based on the FCA model presented in the previous section. Since the universality in analyzing the DAB converter is the unique feature of FCA, a globally applicable solution of DAB modulation for efficient operation is obtained in this section. For implementation of the proposed scheme, a voltage-loop controller of FDM with a simple structure is designed, which is implemented on a digital processor. A small-signal model of the DAB converter with FDM is derived for a stable controller design.

A. Modulation Principle

FDM computes an optimal set of the modulation signals in the fundamental component domain. The objective of the optimal solution is to minimize the magnitude of the inductor current given in (12). The modulation scheme of FDM exploits variables $d_{1,\alpha}$, $d_{1,\beta}$, $d_{2,\alpha}$ for the optimal solution in the way described below. After the calculation, the variable set $d_{1,\alpha}$, $d_{1,\beta}$, $d_{2,\alpha}$ is translated into d_1, d_2, ϕ in the time domain for PWM gating using the relation in (5).

Given V_i, V_o, P_o, L, and f_s, the current minimization problem can be mathematically formulated as

$$\begin{aligned} &\text{minimize } \; d_{1,\beta}^2 + (d_{1,\alpha} - M \cdot d_{2,\alpha})^2 \\ &\text{subject to } \; d_{1,\beta} d_{2,\alpha} = \frac{2X_L P_o}{V_i V_o} \\ &\qquad 0 \le d_{1,\alpha}^2 + d_{1,\beta}^2 \le \frac{16}{\pi^2} \\ &\qquad -\frac{4}{\pi} \le d_{2,\alpha} \le \frac{4}{\pi}. \end{aligned} \tag{14}$$

According to the analytic solution of the constrained optimization problem in (14) derived in Appendix A, the objective function is minimized when

$$D_{2,\alpha} = \frac{4}{\pi}. \tag{15}$$

Then, the problem is reduced to 2-D variable case where D_2 is fixed at 0.5 as

$$D_2 = \frac{1}{\pi} \sin^{-1}(1) = \frac{1}{2}. \tag{16}$$

The power and the current equations in (11) and (12) are reduced, respectively, to

$$P_o = \frac{2}{\pi} \frac{V_i \cdot V_o}{X_L} D_{1,\beta} \tag{17}$$

and

$$\|I_L\| = \frac{V_i}{X_L} \sqrt{D_{1,\beta}^2 + (D_{1,\alpha} - 4M/\pi)^2}. \tag{18}$$

The optimal solution is now given by solving the minimization of (18) constrained by (17). The solution of the optimization problem is obtained as

$$D_{1,\alpha}^* = \frac{4}{\pi} M \tag{19}$$

and

$$D_{1,\beta}^* = \frac{\pi}{2} \frac{P_o \cdot X_L}{V_i \cdot V_o} = \frac{\pi}{2} \frac{I_o \cdot X_L}{V_i} \tag{20}$$

where $D_{1,\alpha}^*$ and $D_{1,\beta}^*$ are the references of $d_{1,\alpha}$ and $d_{1,\beta}$ for the optimal operation. The modulation scheme has two degrees of freedom $d_{1,\alpha}$ and $d_{1,\beta}$. They contribute to current minimization and power balance, respectively. It is seen from (19) that the FDM solution achieves the minimized current when $d_{1,\alpha}$ is equal to $4M/\pi$ which sets the β-component current in (10) to zero to minimize (18). The minimum conduction is realized by adjusting $d_{1,\alpha}$ with respect to the voltage gain information. On the other hand, from (20), $d_{1,\beta}$ should satisfy the power-related

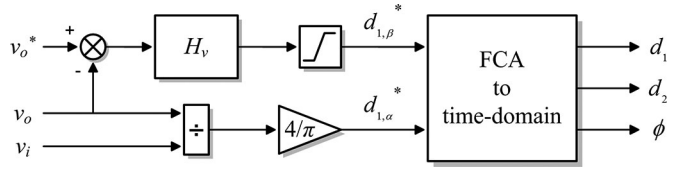

Fig. 4. Block diagram of the voltage-loop controller of the proposed FDM.

equation in (17). The output regulation can be achieved by a voltage-loop controller using a single variable $d_{1,\beta}$.

B. Controller Structure

The controller diagram of FDM is shown in Fig. 4. The sensed output voltage v_o is compared to the reference voltage v_o^*. The voltage loop compensator H_v produces $d_{1,\beta}$ reference to regulate the output voltage. For the minimal conduction, $d_{1,\alpha}$ is computed from the voltage information or given as a constant for a fixed output voltage as in (19). From the relation in (5), the duty ratio signals in the time domain, d_1, d_2, and ϕ, are obtained as

$$\begin{aligned} d_1 &= \frac{1}{\pi}\sin^{-1}\left(\frac{\pi}{4}\sqrt{d_{1,\alpha}^2+d_{1,\beta}^2}\right) \\ d_2 &= 0.5 \\ \phi &= \frac{1}{2\pi}\tan^{-1}\left(d_{1,\beta}/d_{1,\alpha}\right). \end{aligned} \tag{21}$$

Since the inverse trigonometric functions such as arcsine and arctangent consume excessively large computational time, in practical implementation these functions are altered by look-up tables.

Using the calculated d_1, d_2, and ϕ, PWM signals are generated and delivered to the switches through a modulator. It is worth to note that the voltage-gain-related term $d_{1,\alpha}^*$ in the controller block can be constant for a fixed input–output operating condition. If the input or the output voltage is needed to be varied according to operating conditions, the controller can adaptively change $4M/\pi$.

One of the advantages of FDM is the simplicity of the controller in modulating the converter to an optimal solution. Since there is no power-dependent term inside the controller to perform the optimal operation, the controller does not need any current information. Only the output voltage sensing is required to regulate the output voltage and to perform the current minimization operation. Furthermore, the computational complexity is comparable to PSM as will be discussed in the following section. FDM does not need offline calculations or mode selections, which guarantees universality of the method regardless of operating conditions. An example of the digital implementation code of the proposed controller is detailed in Appendix B.

C. Operation of FDM at High Power Range

Maximum transferrable power of the DAB converter is achieved when $d_1, d_2, \phi = 0.5, 0.5, 0.25$. When using FDM, for M smaller than one, the reference of the $d_{1,\alpha}$ is given from (19) as

$$d_{1,\alpha}^* = \frac{4}{\pi}M < 1. \tag{22}$$

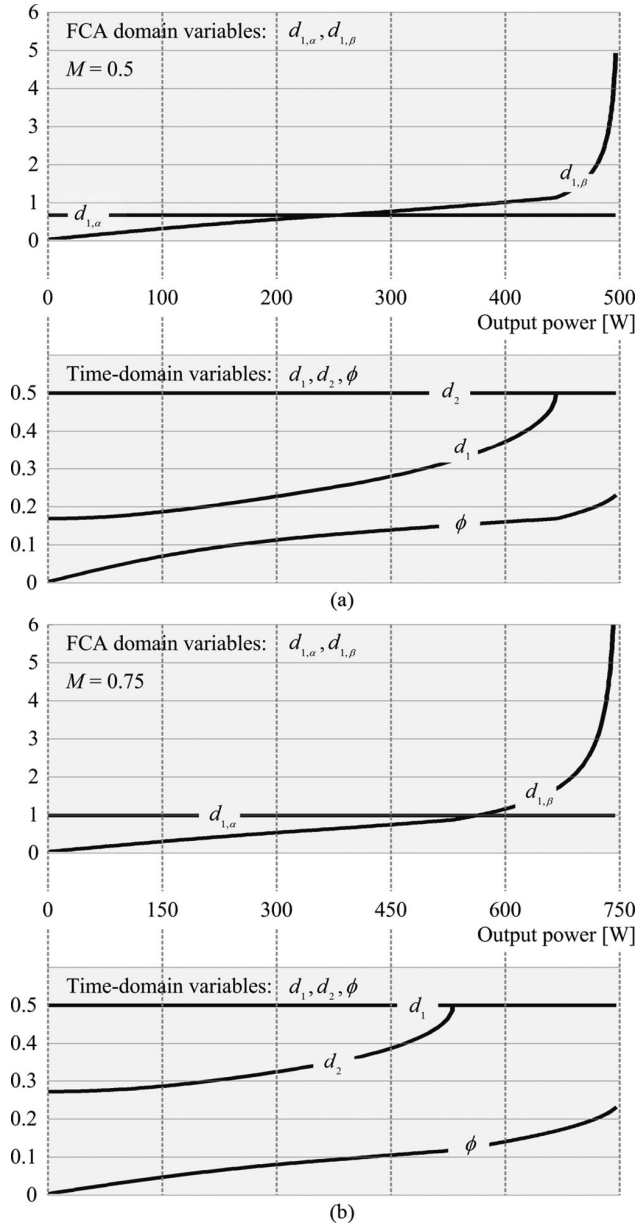

Fig. 5. Operating points of PWM variables in the FCA domain and time domain for (a) $M = 0.5$ and (b) $M = 0.75$.

Theoretical maximum values of $d_{1,\beta}$ is constrained by

$$d_{1,\beta} \le \sqrt{\frac{16}{\pi^2} - \left(d_{1,\alpha}^*\right)^2} = \frac{4}{\pi}\sqrt{1-M^2}. \tag{23}$$

Then, the range of ϕ is obtained as

$$\begin{aligned} \phi &\le \frac{1}{2\pi}\tan^{-1}\left(\frac{d_{1,\beta,\max}}{{d_{1,\alpha}}^*}\right) \\ &= \frac{1}{2\pi}\tan^{-1}\left(\frac{\sqrt{1-M^2}}{M}\right) < 0.25. \end{aligned} \tag{24}$$

In (24), the maximum value of ϕ is smaller than 0.25, which means that the maximum transferrable power is limited. However, using the proposed controller structure, the operating region of $d_{1,\beta}$ is extended until ϕ reaches 0.25. Fig. 5(a) and (b) shows the evolutions of PWM variables in FCA and time domain

according to the output power when M is 0.5 and 0.75, respectively. It is shown that d_1 and ϕ increase from the light load operating range as $d_{1,\beta}$ increases until d_1 reaches 0.5. As load increases further, $d_{1,\beta}$ rises larger than the theoretical value in (23) to increase ϕ to the maximum level. In this way, FDM utilizes the maximum transferrable power of the DAB converter.

D. Small-Signal Model

To design the compensator of the voltage-loop controller, small-signal modeling of the DAB converter with FDM is necessary. To incorporate the dynamics of the inductor current, full-order modeling has been addressed to model the fundamental component of the inductor current [9]. The small-signal model of the DAB converter with FDM is formulated using the dynamic equations in (7) and (9). Assuming a constant input voltage, the control variable is $d_{1,\beta}$. Other duty ratio signals areassumed to be fixed at $d_{1,\alpha} = 4M/\pi$ and $d_{2,\alpha} = 4/\pi$. The model is, therefore, reduced to

$$\begin{aligned} L\frac{di_\alpha}{dt} - \omega L i_\beta &= \frac{4M}{\pi}v_i - \frac{4}{\pi}v_o \\ L\frac{di_\beta}{dt} + \omega L i_\alpha &= d_{1,\beta}v_i \\ C\frac{dv_o}{dt} &= \frac{2}{\pi}i_\alpha - \frac{v_o}{R}. \end{aligned} \tag{25}$$

As seen from (25), there is no direct relationship between the control variable $d_{1,\beta}$ and v_o. That is, without incorporating the current dynamics, the model cannot derive the control-to-output transfer function which is essential for a voltage-loop design. Hence, small-signal characteristics of FDM can only be modeled using the full-order modeling method which includes the α- and β-component current dynamics as well as the voltage dynamics. After perturbing (25) around the operating point, the small-signal model is formulated as

$$\frac{d}{dt}\begin{bmatrix} i_\alpha \\ i_\beta \\ v_o \end{bmatrix} = \begin{bmatrix} 0 & \omega & -4/\pi L \\ -\omega & 0 & 0 \\ 2/\pi C & 0 & -1/RC \end{bmatrix}\begin{bmatrix} i_\alpha \\ i_\beta \\ v_o \end{bmatrix} + \begin{bmatrix} 0 \\ V_i/L \\ 0 \end{bmatrix} d_{1,\beta}. \tag{26}$$

The transfer function from the control variable $d_{1,\beta}$ to the output voltage v_o is obtained as

$$G_{vd}(s) = \frac{\dfrac{2\omega}{\pi LC}}{s^3 + \dfrac{1}{RC}\cdot s^2 + \left(\omega^2 + \dfrac{8}{\pi^2 LC}\right)\cdot s + \dfrac{\omega^2}{RC}}. \tag{27}$$

The transfer function in (27) has a pole and a double pole at low- and high-frequency region, respectively. Fig. 6 shows the bode plots of the control-to-output transfer functions obtained from the small-signal analysis in (27) and from a simulation result using PSIM. The bode plots are drawn for a frequency range from 1 Hz up to half of the switching frequency in which the double pole at the high frequency does not appear. The results strongly coincide for the broad frequency region except for the half of the switching frequency region where the PSIM model is inaccurate. Consequently, the voltage loop can be designed with a simple PI controller to stabilize the converter.

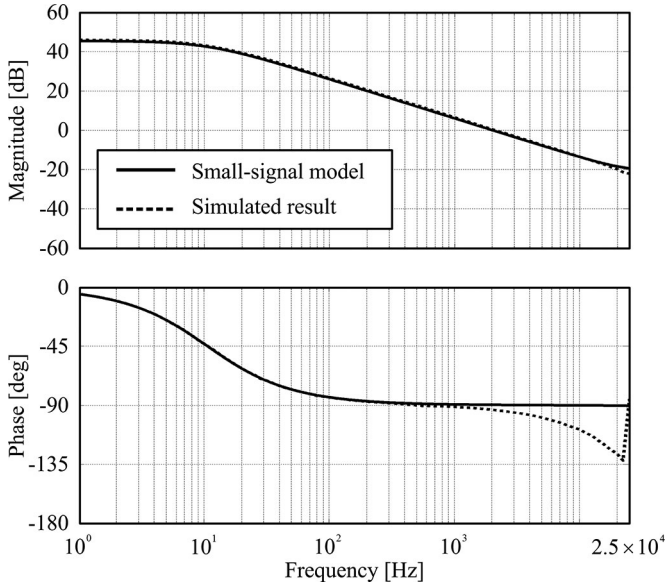

Fig. 6. Bode plots of the control-to-output transfer function from the small-signal model (bold) and a simulation result (dotted).

IV. Operational Characteristics

The optimality obtained by FDM differs from other modulation methods in the fact that the analysis for derivation of optimal operation is approximated with fundamental components. FDM has distinctive features in operational characteristics. The proposed method is compared to recent related modulation schemes in various aspects. RMS current level and ZVS characteristics are analyzed and loss breakdown is performed for comparison of FDM against the previous works.

A. Qualitative Characteristics

Under rigorous analysis, Krismer *et al.* in [22]–[25] have suggested sophisticated modulation schemes manipulating the 3-D duty signals d_1, d_2, ϕ. Among those works, the online methods in [23] and [24] perform improved modulation schemes without offline calculations. A qualitative comparison between the proposed FDM and previous works including the simplest PSM method is shown in Table II. Main properties of the previous works are as follows.

1) *PSM scheme:* The phase ϕ between the primary and the secondary sides are shifted to regulate the output voltage. Control variable is ϕ, while d_1 and d_2 are fixed at 0.5. Computational time required for a single switching cycle is 2.8 μs using a 75-MHz CPU clock. It benefits from the simple control structure, while it suffers from, as mentioned, a large circulating current and hard switching at light load and nonunity voltage gain conditions.
2) *PWM control with composite scheme* [23]*:* Objective of the method is minimization of rms current at low power range and ZVS achievement at high power range. It operates in TRM mode at light-load condition. Such discontinuous conducting mode can achieve minimal rms current by reducing the circulating currents. Although ZVS is not achieved, the switches are turned OFF with zero current. For high power range, the modulation scheme in [23] is

TABLE II
QUALITATIVE CHARACTERISTICS OF THE PROPOSED AND THE RECENT RELATED WORKS

Principles	Variables	Computational time[1), 2)]	
	PSM (phase-shift modulation) scheme		
Phase-shift	$\phi = \text{controlvariable}$ $d_1 = 0.5, \quad d_2 = 0.5$	2.8 μs	1 times
	Proposed FDM		
I_{rms} minimization	$d_{1,\beta} = \text{control variable}$	7.3 μs	2.6 times
FCA based	$d_{1,\alpha} = \frac{4}{\pi}M, \quad d_2 = 0.5$	5.2 μs[3)]	1.8 times[3)]
	PWM control with composite scheme [23]		
TRM at low power range	$\phi = \text{control variable}$	5.7 μs	2.0 times
ZVS at high power range	$d_1 = \begin{cases} 2M^*\phi, & 0 \leqslant \phi \leqslant \frac{1-M}{4} \\ \frac{1}{2} + \frac{1}{2M^*}(4\phi - 1), & \frac{1-M}{4} < \phi \leqslant \frac{1}{4} \end{cases}, d_2 = \begin{cases} M^*\phi, & 0 \leqslant \phi \leqslant \frac{1-M}{4} \\ \frac{1}{2}, & \frac{1-M}{4} < \phi \leqslant \frac{1}{4} \end{cases}$		
Time domain based	$M^* := \frac{M}{1-M}$		
	PWM plus phase-shift control: Fundamental-Optimal Strategy [24]		
Q minimization	$\phi = \text{control variable}$	4.8 μs	1.7 times
FCA based Limited power range	$d_1 = \frac{1}{2} - \frac{\cos^{-1}(M)}{2\pi}, \quad d_2 = 0.5$	3.6 μs[3)]	1.3 times[3)]

[1)] Computational times are calculated based on 75-MHz CPU clock.
[2)] Calculation of computational time may vary in certain range according to implementation.
[3)] Reduced computational time is obtained using look-up tables.

formulated to satisfy a marginal ZVS condition. Computational time of the scheme is measured to be 2.0 times of PSM.

3) *Fundamental-optimal strategy* [24]*:* Objective of the scheme is minimization of reactive power, Q, in the FCA domain which is equivalent to the rms minimization strategy of the proposed FDM. However, in [24], an approximated solution has been applied for ease of implementation. d_1 is fixed at the entire load condition given a voltage gain. Hence, rms current level is not optimized, and, also, maximum transferrable power is limited to a reduced level. Computational time is 1.7 times of PSM, while it can be reduced to 1.3 times using look-up table for arccosine function.

Computational complexities of the methods are compared against the conventional PSM which is the simplest modulation scheme. PSM method is assumed to be implemented using a single voltage loop to regulate the phase ϕ as detailed in Appendix B. Computational burden of FDM is 2.6 times of PSM. As explained in the previous section, the inverse trigonometric functions (arcsine and arctangent) used in the proposed scheme mainly increase the computational complexity. It can be reduced to 1.8 times of PSM using look-up tables in implementation.

The modulation schemes listed in Table II including FDM require only the input and the output voltage information. They are independent to circuit parameters as well as output current information. The computational times for implementation are in acceptable range compared to the simplest PSM method. Also, it is worth to note that FDM and the other modulation strategies operated exactly same as PSM when $M = 1.0$.

B. Steady-State Analysis: RMS Current

Since FDM is formulated based on the FCA domain, the solution in (19) and (20) does not guarantee actual minimized rms value of the inductor current in time domain. In Fig. 7, rms current levels of the various modulation strategies including FDM are shown. The rms currents are calculated using time-domain-based numerical analysis for the control scheme listed in Table II.

As seen in Fig. 7(a) and (b), a PSM method has the highest circulating current for light-load operations as expected especially at $M = 0.5$ and 0.625. The time-domain-based current minimization strategy of [23] achieves the lowest rms current level at low power range. Although FDM maintains low rms current for large operating conditions, at the very light-load condition, the rms current level is higher than [23]. The method in [24] shows relieved rms current level compared to PSM. However, its current minimization strategy does effectively reduce the rms level for low and high power ranges.

In Fig. 8, a few examples of simulated waveforms of the inductor current using FDM and TRM in [23] are shown. Based on the observation that the circulating currents of the DAB converter at light-load operation is increased excessively compared to the delivered power, TRM permits an off-state interval where both primary- and secondary-side currents are freewheeling.

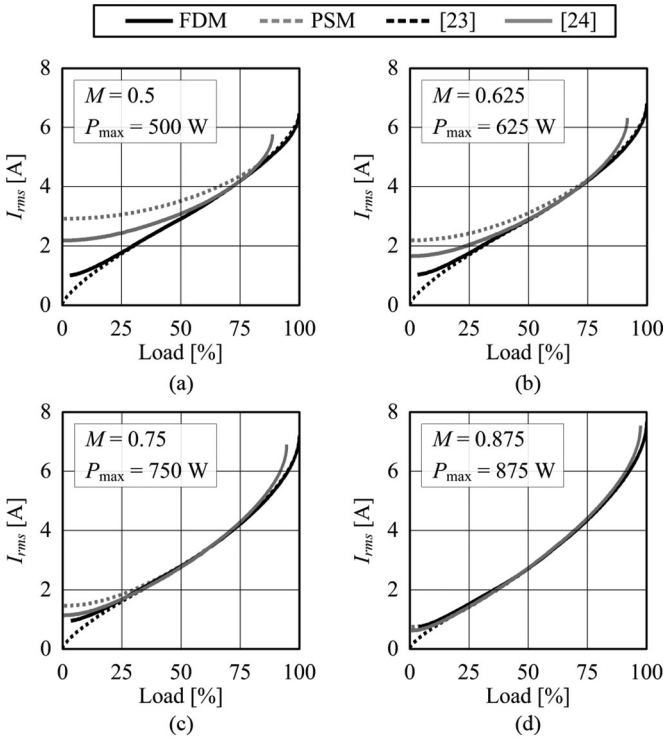

Fig. 7. RMS currents of various modulation schemes for (a) $M = 0.5$, (b) $M = 0.625$, (c) $M = 0.75$, and (d) $M = 0.875$.

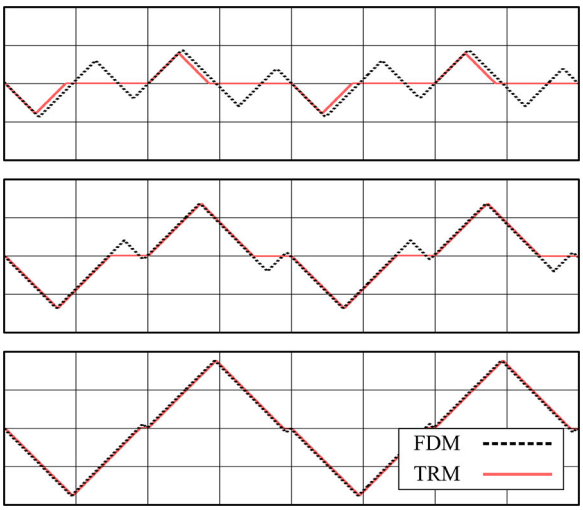

Fig. 8. Examples of inductor current waveforms at light- load operation using FDM (dotted black) and TRM in [23] (bold red).

Hence, the circulating current is eliminated and the secondary-side switches are turned OFF with zero current switching. It can be seen from Fig. 8 that TRM has discontinuous conduction intervals, while FDM circulates the current. Since FDM does not have the off-state during its operation, the additional circulating current is inevitable.

C. Steady-State Analysis: ZVS Range

When operating in unity voltage gain, MOSFETs of a phase-shifted DAB converter are turned on with ZVS. However, it is well known that the ZVS range of the DAB converter is limited as voltage gain deviates from unity and load decreases. For a proper ZVS, the inductor current should discharges the output capacitance of the MOSFETs during the commutation period of switches. Neglecting the winding capacitance of the transformer, condition for ZVS operation is given as

$$Li_L^2 > 2C_{oss}V_D^2 \tag{28}$$

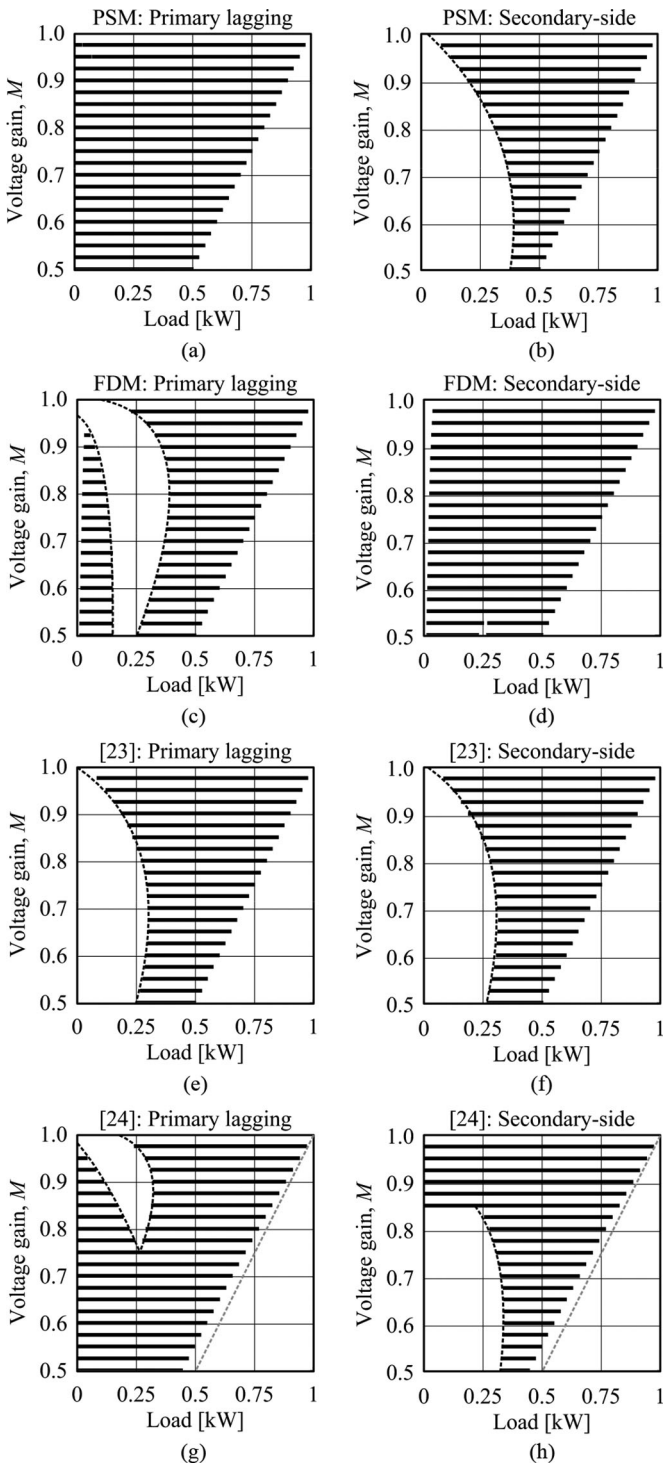

Fig. 9. ZVS ranges of primary-side lagging leg and secondary-side legs using (a) and (b) PSM, (c) and (d) FDM, (e) and (f) method in [23], and (g) and (h) method in [24], respectively, with $C_{oss} = 100$ pF.

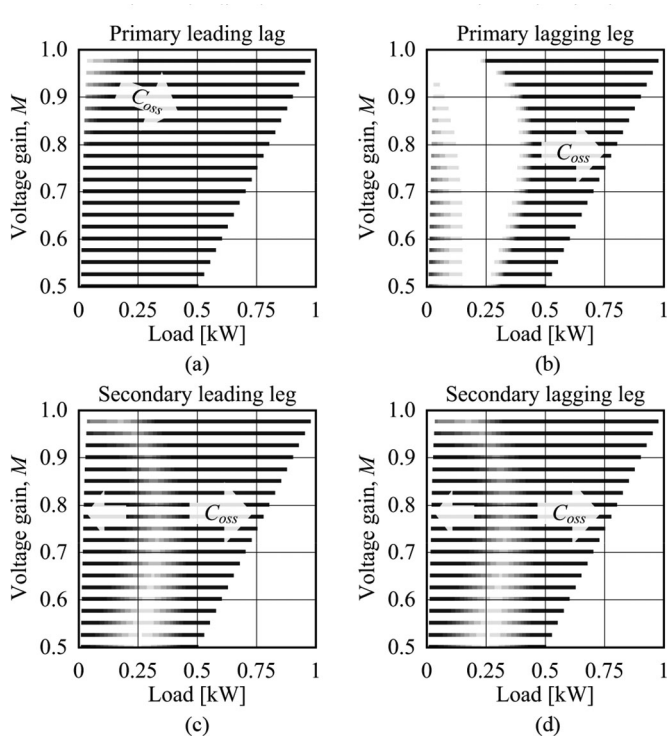

Fig. 10. ZVS characteristics of FDM with increasing C_{oss} from 100 to 6300 pF of (a) primary-side leading leg, and (b) lagging leg, and (c) secondary-side leading leg, and (d) lagging leg.

where C_{oss} is output capacitance of the MOSFET and V_D is the drain-source voltage during turn-off period [27]. The ZVS characteristics are estimated assuming that the leakage inductance and the output capacitances form a resonant circuit during the dead time interval neglecting the secondary-side voltages. Fig. 9 shows ZVS ranges of the various modulation methods including FDM assuming $C_{oss} = 100$ pF. By numerically analyzing the operating characteristics at power-gain domain, the ZVS condition in (28) is examined. It should be noted that the tendency observed in this ZVS analysis result is independent to the converter design parameters.

The black bold lines in Fig. 9 indicate operating points with ZVS turn-on. Using the strategies in Table II, switches of primary-side leading leg are always turned-on with ZVS, and leading and lagging legs on secondary side exhibit the identical ZVS characteristics. Hence, in Fig. 9, only the ZVS ranges of primary-side lagging leg switches, and secondary-side switches are depicted.

As in Fig. 9(b), the conventional PSM method suffers from secondary-side hard switching which have been well known to be a major factor of low efficiency at light load and low *M*. The proposed FDM shows non-ZVS range in Fig. 9(c) on primary-side lagging leg over the medium power range, while other switches are operated in ZVS. It is seen from Fig. 9(e) and (f) that the PWM scheme in [23] has non-ZVS region at low power operation. It is mainly due to the fact that the objective of TRM operation at light-load condition is on the minimization of rms current not on the ZVS of switches. For medium to high power ranges, all switches are in soft-switching region as it intended. However, the soft-switching strategy in [23] is

TABLE III
CONVERTER SPECIFICATIONS FOR LOSS ANALYSIS AND EXPERIMENT

	Parameter		Value
Power	Input voltage	V_i	200 V
	Output voltage	V_o	200 to 400 V
	Voltage gain, $V_o/V_i/N$	M	0.5 to 1.0
	Theoretical $P_{\max}$	$P_{\max}$	500 to 1000 W
	Switching frequency	f_s	50 kHz
	Output capacitance	C	220 μF
Magnetics	Inductor	L	95.6 μH
		R_s	120 mΩ
		Turns	40
		Air-gap	3 mm
	Transformer	L_{lk}	2.96 μH
		L_m	814 μH
		Turn ratio	11:22
		$R_{s,p}$	30 mΩ
		$R_{s,s}$	700 mΩ
Switch	Primary side	IPP50R140CP	
		$R_{DS,on}$	140 mΩ
		C_{oss}	110 pF
	Secondary side	STP11NM60	
		$R_{DS,on}$	450 mΩ
		C_{oss}	230 pF
Controller		TMS320F28335	

a marginal condition derived in time domain which does not guarantee ZVS operation for high C_{oss}. In Fig. 9(g) and (h), ZVS characteristics of the modulation method in [24] show non-ZVS region of primary-side lagging leg at high *M*, and secondary-side legs at low *M*, respectively. It is also noted that the maximum transfer power is reduced than the other modulation methods [see dotted gray line in Fig. 9(g) and(h)].

ZVS characteristic of the proposed FDM is further investigated regarding various output capacitance options. As C_{oss} increases, the ZVS range is inevitably decreased since it requires more energy to fully discharge the capacitance. In Fig. 10, the ZVS ranges of the switches on each leg are drawn where the ZVS range (black lines) narrows as C_{oss} increases. As seen in Fig. 10(a), (c), and (d), the ZVS ranges of primary-side leading leg and secondary-side legs are relatively well preserved under increase of C_{oss}. However, the primary-side lagging leg in Fig. 10(b) shows large non-ZVS range for high C_{oss}, which requires a careful circuit design and gating scheme.

D. Steady-State Analysis: Loss Breakdown

Based on the previous analysis on rms currents and ZVS characteristics of the DAB converter for various modulation schemes, loss analysis at various operating conditions is performed. Specified circuit parameters for loss analysis and experimental verification are given in Table III where R_s is series resistance, and L_{lk} and L_m are leakage and magnetizing inductance of the transformer. For the loss analysis, the magnetizing inductance is assumed infinite.

Based on the traditional loss analysis method, a loss model for the DAB converter has been derived [26]. Power loss mechanism is composed of three main loss factors: switching losses, conduction losses, and core losses. To take account of the switching characteristics of switches, turn-on loss is equated

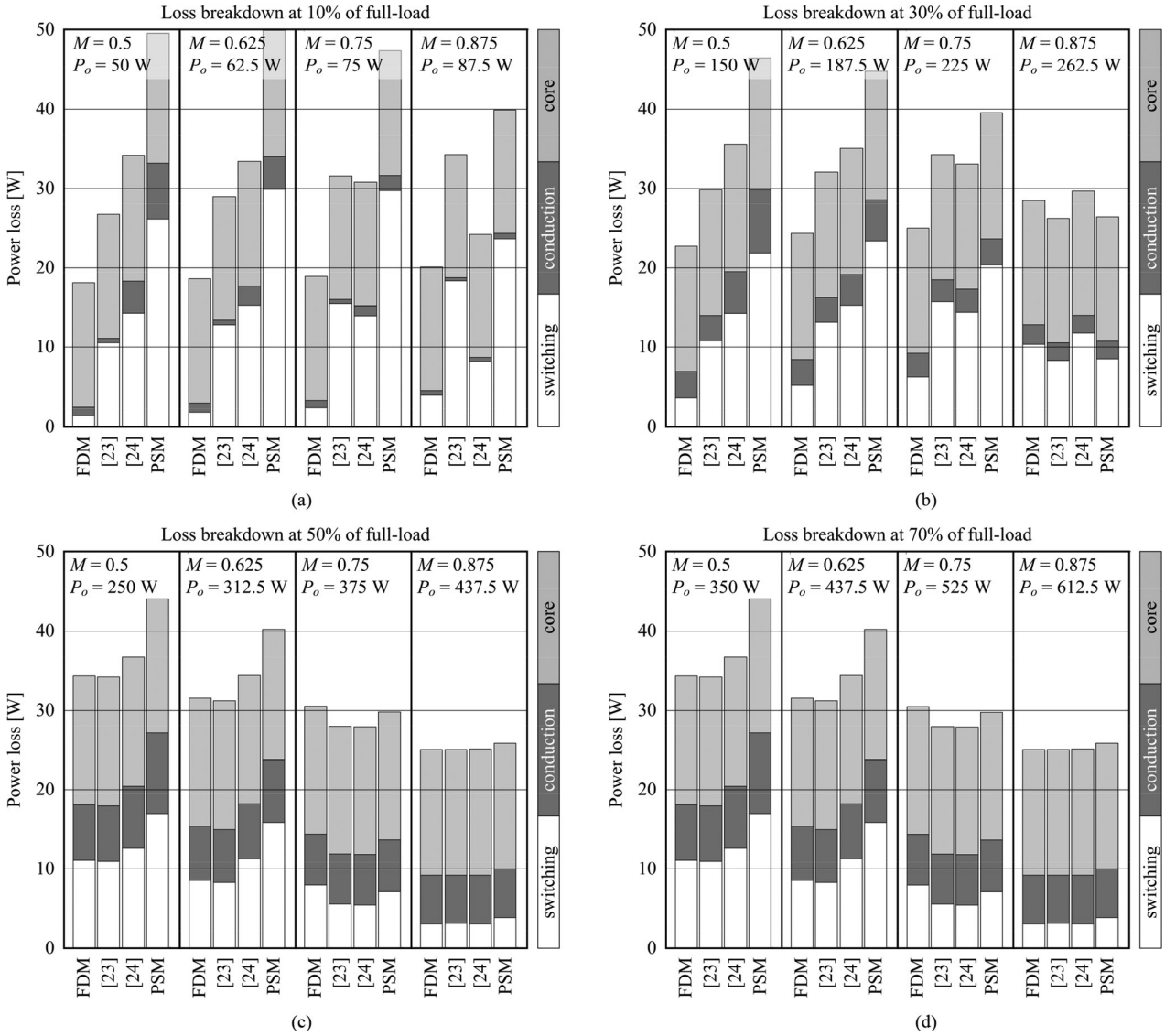

Fig. 11. Power loss analysis for various load and voltage gain conditions using modulation schemes based on FDM, [23], [24], and PSM at (a) 10%, (b) 30%, (c) 50%, and (d) 70% of full load.

regarding 1) the overlap of rising and falling slopes of drain-source voltage and drain current, and 2) capacitive discharge energy. Using the result delivered in Fig. 7, conduction losses are calculated as the sum of $R_{DS,\mathrm{on}}$ conduction losses and copper losses of the magnetic components. Finally, core loss estimation is performed using the Steinmetz equation with the parameters from core material datasheet.

Fig. 11 shows the results of the loss analysis for various voltage gain and load conditions under the modulation schemes based on FDM, PSM, [23], and [24]. Before discussion on the loss breakdown result, it should be addressed that:

1) Maximum transfer power of the prototype DAB converter varies from 500 to 1000 W according to the output voltage ranging from 200 to 400 V.
2) The results for $M = 1.0$ is excluded since, as discussed previously, all of the four modulation strategies operates effectively in the same way as PSM.
3) For the same reason, loss analysis results at full-load condition are not shown.
4) The core losses are not optimized. In actual operation of the circuit, flux density of the transformer reaches high level and it can be relieved in a proper magnetic design which, however, is beyond the scope of the paper.
5) Efficiency at each operating point can be estimated from the figure. For example, for FDM operating at 10% load and $M = 0.5$ in Fig. 11(a), the efficiency is

$$\eta = \frac{\text{output power}}{\text{output power} + \text{total loss}} \times 100 = \frac{50}{50 + 18} \times 100 = 73\%. \tag{29}$$

Significant remarks deduced from the loss analysis results are as follows.

1) *Operation of PSM:* The conventional PSM method exhibits moderate efficiency at heavy load condition in Fig. 11(d). However, as load decreases, the switching and conduction losses excessively increase which lead to about 50% of efficiency at 10% load and $M = 0.5$.

This is due to large circulating current and hard-switching condition on secondary-side switches.

2) *FDM and* [23] *at light load:* At light-load condition in Fig. 11(a), the method in [23] achieves minimum rms current by using the TRM operation, therefore having the lowest conduction loss. However, the absolute value of the conduction loss accounts for few percentages of the total losses. Also, since it does not have ZVS property, the capacitive energy across the switches is dissipated which result in increased switching losses. For these reasons, although FDM has higher conduction loss, it shows superior performance at light load in the aspect of overall efficiency.
3) *Non-ZVS range of FDM:* The loss analysis results in Fig. 11 show that the switching losses of FDM are smaller than or similar to the other methods for large operation range. However, FDM has non-ZVS range of primary-side lagging leg switches as discussed previously. In Fig. 10(c), non-ZVS range of the switch is estimated to be centered on power range between 300 and 500 W, and voltage gain between 0.7 and 0.9. It can be seen from Fig. 11(c) and (d) that the switching losses of FDM are higher compared to the other modulation methods for $M = 0.75$ and 50% and 70% load conditions.
4) *Voltage gain dependence of* [24]*:* According to the results in Fig. 11(c) and (d), the method in [24] shows moderate performance at $M = 0.75$ and 0.875. However, as explained in [24], for a fixed voltage gain, the [24] method is operated with a constant d_1. As discussed previously in Fig. 7(a) and (b), this simplified strategy does not minimize the rms current for low-voltage gain condition. Moreover, as in Fig. 9(g) and (h), the secondary-side switches suffer from hard switching at light-load condition. Since the rms current and the ZVS characteristics are not optimized, for most of operating points, FDM or the [23] method gives better modulation option with lower power losses.

V. Experiments

A prototype DAB converter was designed for verification of the proposed scheme. Salient parameters of the prototype converter are listed in Table III. The theoretical maximum power is ranging from 500 to 1000 W according to the output voltage. Before demonstration of the results, it is worth to note that:

1) The following waveforms were obtained from a closed-loop converter for output voltage regulation based on FDM, PSM, and the methods in [23] and [24].
2) For finite magnetizing inductance and commutation time, practical maximum transfer power is smaller than $P_{\max}$. In this paper, efficiencies were measured up to 91% load of the theoretical maximum output power.

A. Steady-State Waveforms

Fig. 12 shows the steady-state waveforms of the primary-side voltage v_1, secondary-side voltage v_2, and the inductor current i_L for various output power. The output voltage was set at 250 V ($M = 0.625$). At a light load of 70 W, as shown in Fig. 12(a), the current waveform had a repetitive triangular shape as discussed previously. For medium-power range of 370 W in Fig. 12(b), d_1 was smaller than 0.5 to minimize the current conduction. For the high-power operation of 520 W, in Fig. 12(c), the proposed FDM worked in the same principle as PSM. Since d_1 and d_2 became 0.5, the number of switching instants during a switching period was reduced to 4.

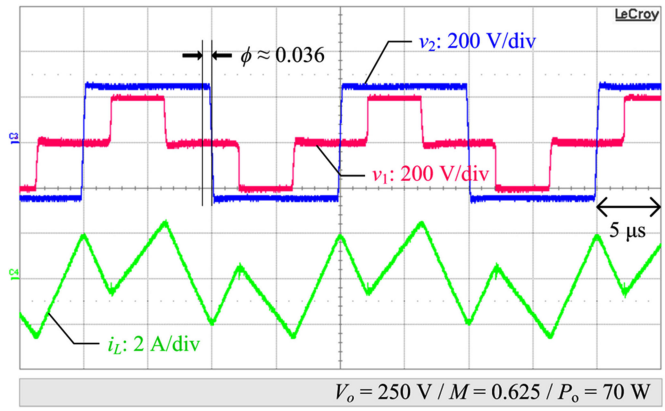

(a)

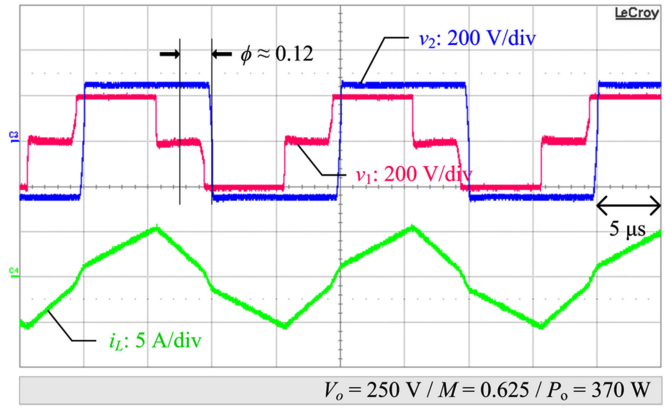

(b)

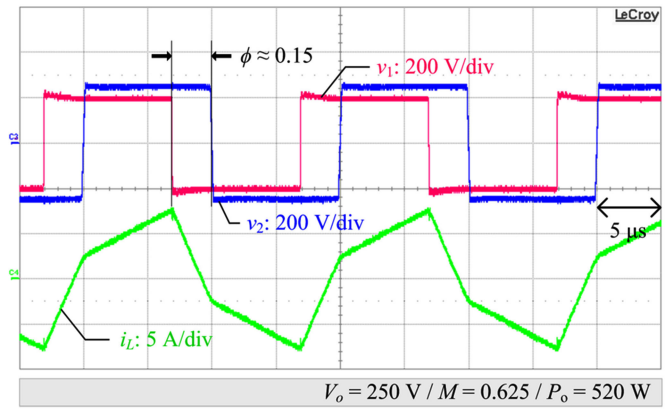

(c)

Fig. 12. Steady-state waveforms of v_1 (red), v_2 (blue), and i_L (green) using the proposed FDM for $M = 0.625$ at (a) 70, (b) 370, and (c) 520 W.

In Fig. 13, the steady-state waveforms of FDM at 11% of loading condition as in Fig. 12(a) are depicted for various voltage gains. The output voltage was varied from 200, 300, 350, to 400 V as $M = 0.5$, 0.75, 0.875, and 1.0 in Fig. 13(a), (b), (c), and

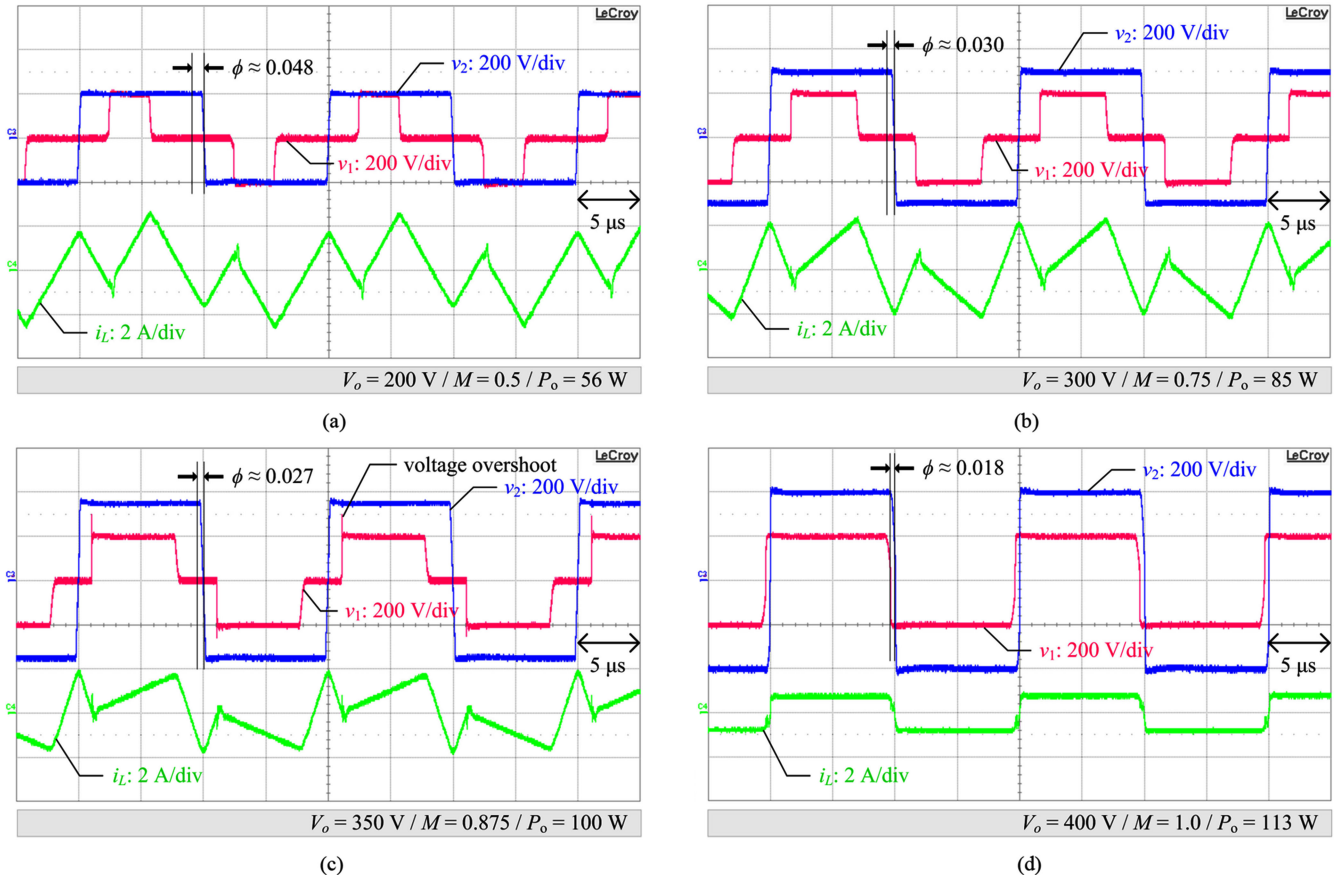

Fig. 13. Steady-state waveforms of v_1 (red), v_2 (blue), and i_L (green) using FDM for various conditions: voltage gains are (a) $M = 0.5$, (b) $M = 0.75$, (c) $M = 0.875$, and (d) and $M = 1$.

(d), respectively. Phase between the primary- and the secondary-side voltages are remained small for light-load operations. As seen from Fig. 13(a), the inductor current flowed in negative direction at turn-on instant of the switches from which ZVS of the entire switches is estimated as explained in Fig. 9. However, in Fig. 13(c), an overshoot voltage on the primary-side voltage was observed at the switching instant of the lagging leg switches. This overshoot was due to the reverse recovery mechanism of the body diode on the hard-switched leg. As discussed, FDM operated in the same way as PSM when $M = 1.0$ as depicted in Fig. 13(d).

B. Additional Waveforms

In principle, the DAB converter works in bidirectional power flow by changing the sign of ϕ. FDM can achieve reverse power flow operation without manipulating the controller structure. When the power flows in negative direction, the control variable $d_{1,\beta}$ becomes negative to satisfy (21) to regulate the output voltage from which ϕ also becomes negative as computed in (22). As shown in Fig. 14, the primary-side voltage v_1 lagged v_2 to achieve the reverse power flow operation with negative phase. The proposed modulation scheme still worked effectively to minimize the conduction level.

In Fig. 15, the TRM operation exploited in [23] is depicted for comparison. The experimental condition is same as the waveform in Fig. 12(a). For an effective visualization of the waveform comparison, the current waveform in Fig. 12(a) is overlapped as a gray line. The inductor current of the TRM stayed at zero level for the discontinuous conduction interval to avoid unnecessary current circulation. Compared to the current waveform of FDM under the same operating condition, the rms current was clearly reduced.

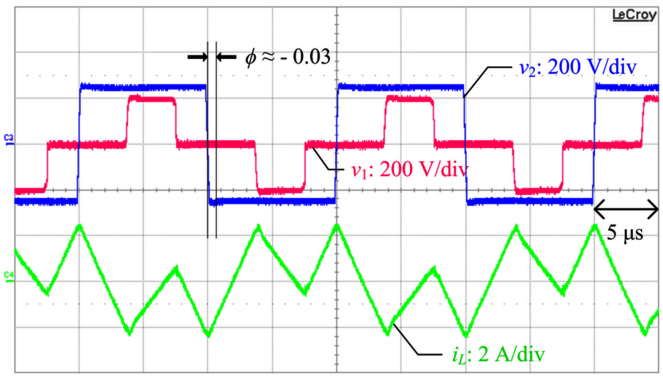

Fig. 14. Reverse power flow operation of FDM: v_1 (red), v_2 (blue), and i_L (green).

Fig. 16 demonstrates the ZVS characteristics of FDM. The current waveform centered in Fig. 16 shows a waveform of the inductor current at 70 W and 250 V which is the same condition with the waveforms in Fig. 12(a). Switching instants of the switches on each leg are marked with dotted circles. In Fig. 16, waveforms of the drain-source voltage v_{ds}, gate-source voltage v_{gs}, and the inductor current i_L at turn-on instants of Q_1,

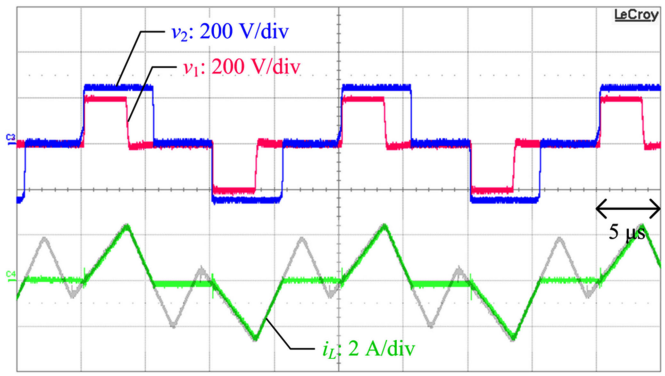

Fig. 15. Steady-state waveforms of v_1 (red), v_2 (blue), and $i_{\rm L}$ (green) using the TRM in [23] overlapped with $i_{\rm L}$ of FDM (gray).

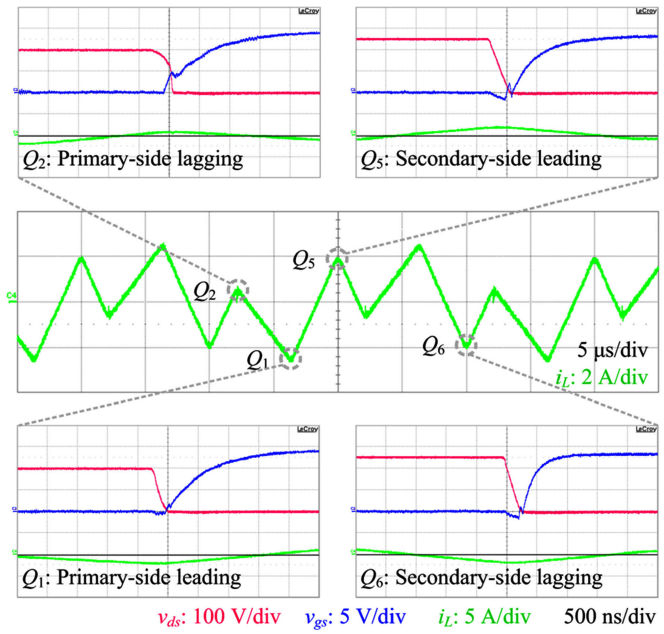

Fig. 16. Inductor current waveform with switching instants marked, and ZVS waveforms of v_{ds} (red), v_{gs} (blue), and i_L (green) of each leg.

Q_2, Q_5, and Q_6 were separately measured. As explained in the previous ZVS analysis, all the legs except for the primary-side lagging leg performed ZVS for almost entire operating range. However, as seen in the ZVS waveform of Q_2, the drain-source voltage of Q_2 did not reach to zero before the rising slope of the gate-source voltage. This is because the inductive energy was not enough to fully discharge the output capacitance of Q_2.

C. Efficiency Curves

In Fig. 17, experimental efficiency curves of FDM, PSM, and the methods in [23] and [24] were depicted. Efficiency data for the curves in Fig. 17 were obtained using a constant-current electric load on the output side. The load current was changed so that the output power varies from 7% to 91% of the theoretical full-load capacity at a given output voltage. Efficiency was measured at every 0.1 A step of the load. With a fixed input voltage of 200 V, the output voltage varied from 200 to 400 V ($M = 0.5 - 1.0$).

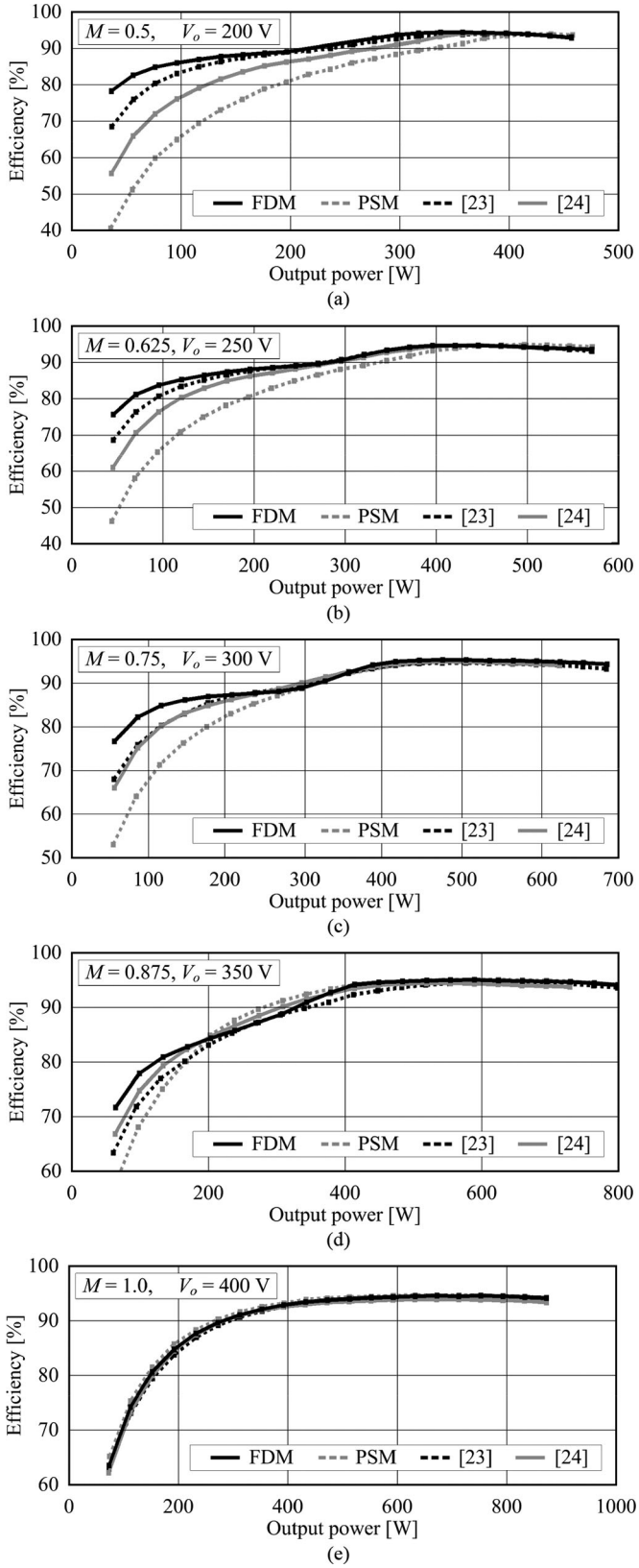

Fig. 17. Efficiency curves of FDM, PSM, [23], and [24] under various voltage gains: (a) $M = 0.5$, (b) $M = 0.625$, (c) $M = 0.75$, (d) $M = 0.875$, and (e) $M = 1.0$.

TABLE IV
LIGH-LOAD EFFICIENCIES AND THEIR IMPROVEMENTS COMPARED TO PSM

Operating Conditions		Efficiency of PSM	Efficiency improvement compared to PSM		
M	Load	PSM	FDM	[23]	[24]
0.5	7%	40.3%	+37.9%	+28.0%	+15.1%
	11%	50.9%	+29.7%	+25.0%	+14.8%
0.625	7%	45.9%	+29.7%	+22.6%	+14.9%
	11%	57.8%	+23.2%	+18.5%	+12.7%
0.75	7%	52.8%	+23.8%	+15.1%	+13.0%
	11%	63.9%	+18.1%	+11.9%	+11.2%
0.875	7%	57.0%	+14.5%	+6.2%	+9.7%
	11%	67.9%	+9.9%	+3.8%	+6.7%

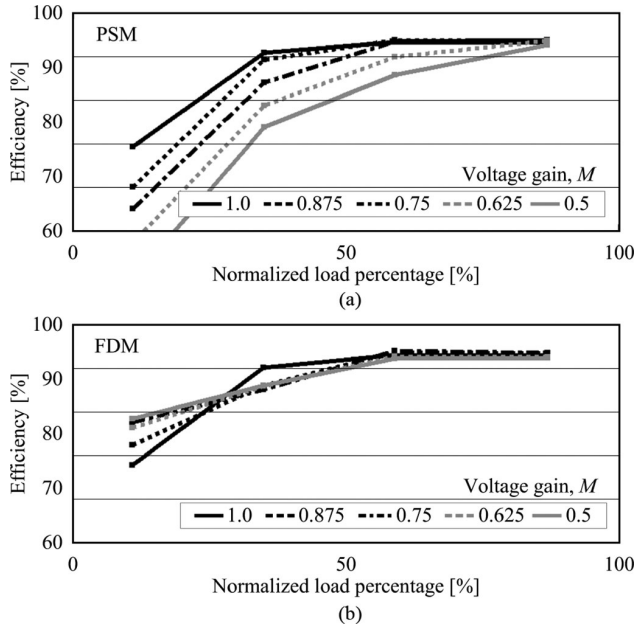

Fig. 18. Normalized efficiency curves of (a) PSM and (b) FDM with respect to voltage gain.

For various voltage gain condition, efficiency of FDM was higher than the other modulation methods for most of the operation points. Especially, at light-load condition, FDM has shown significant efficiency improvement compared to the conventional schemes. For $M = 1.0$ in Fig. 17(e), four of the modulation method have shown identical performances as described previously.

Table IV detailed efficiency improvements of the modulation schemes at light-load condition from the efficiency results in Fig. 17. Compared to PSM that had poor light-load efficiency, especially for low *M*, the other methods have shown improved energy conversion performances. FDM exhibited an excellent performance at light-load and low-voltage gain condition where 37.9% of efficiency improvement was measured at 70 W and $M = 0.5$. At this operation condition, the efficiency of FDM was about 10% and 20% greater than the methods in [23] and [24], respectively.

However, efficiency drops of FDM at the medium power range were seen from Fig. 17(c) and (d). At these operating conditions, the switching losses of the primary-side lagging leg switches mainly contributed to the efficiency deterioration. In result, at the worst case of FDM with 300 W and $M = 0.875$, 2.5% efficiency drop compared to the other schemes was observed.

Experimental efficiencies at specific operating points (11%, 35%, 60%, and 85% load) using the conventional PSM and FDM are depicted in Fig. 18 for various *M*. It can be seen from Fig. 18(a) that the efficiency of the conventional PSM at light-load condition decreased dramatically as *M* decreases. In other words, the conventional method depends highly on the operating condition. As mentioned previously, PSM under low *M* suffers from high circulating current and hard switching at light load. Consequently, operating range of *M* should be designed close to 1 when operating a DAB converter with PSM.

However, as seen from Fig. 18(b), FDM has shown relatively consistent efficiency regardless of voltage gain. The curves were relatively independent to the operating conditions. Moreover, while the efficiency of PSM increased monotonically as load increased, FDM maintained moderately high efficiency from mid- to high-power range. At low power range, there was a tendency where efficiency increases for lower *M*. The converter design with lower *M* would be an optimal choice for the application where light-load operation dominates. This result implies that the proposed method is advantageous for wide-voltage-range applications, such as battery conditioning system. Design of the converter specification, especially the inductance and the turn ratio, would require a careful concern since, not like PSM, the operating characteristic of FDM is not always efficient for $M = 1.0$.

VI. CONCLUSION

In this paper, an optimal modulation scheme for the DAB converter is proposed based on the FCA. By modulating the duty ratio signals in the fundamental component domain, the minimum-level circulating current was acquired with a single control variable. Hence, the controller structure of the proposed FDM becomes significantly simpler, while maintaining the high efficiency over the entire operating region with computational complexity only 1.8 times of the conventional PSM scheme. By developing the loss model of the DAB converter based on the state-state analysis on rms current and ZVS characteristics, performances of FDM were compared to various modulation schemes. Efficiency measurements were conducted for FDM and other recent related works under various operating conditions. Efficiency improvement of the proposed FDM has reached 10%–38% at light-load condition compared to the conventional modulation methods.

APPENDIX A

The current minimization problem in (14) is as follows:

$$\begin{aligned} \text{minimize} \quad & d_{1,\beta}^2 + (d_{1,\alpha} - M \cdot d_{2,\alpha})^2 \\ \text{subject to} \quad & d_{1,\beta} d_{2,\alpha} = \frac{2X_L P_o}{V_i V_o} \\ & 0 \le d_{1,\alpha}^2 + d_{1,\beta}^2 \le \frac{16}{\pi^2} \\ & -\frac{4}{\pi} \le d_{2,\alpha} \le \frac{4}{\pi}. \end{aligned} \tag{A.1}$$

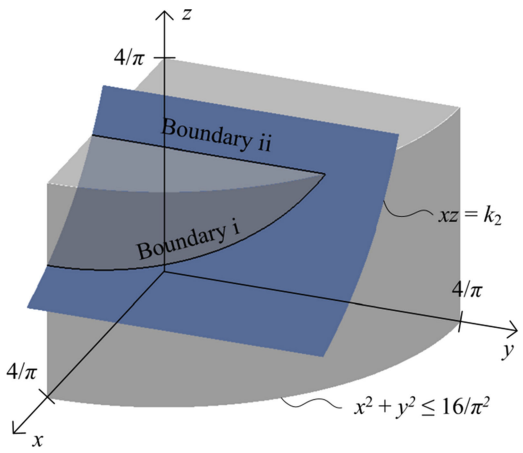

Fig. A.1. Geometry of the minimization problem when $k_2 = 1$.

The problem can be translated into a simpler form as

$$\begin{aligned} \text{minimize} \quad & f := x^2 + (y - k_1 z)^2 \\ \text{subject to} \quad & xz = k_2 \\ & 0 \le x^2 + y^2 \le \frac{16}{\pi^2} \\ & 0 \le z \le \frac{4}{\pi} \end{aligned} \tag{A.2}$$

where $0 \le k_1 \le 1$ and $0 \le k_2 \le 16/\pi^2$. Given k_1 and k_2, we will find the point $(x,\ y,\ z)$ that minimizes the objective function f. Geometry of (A.2) is described in Fig. A.1 for $k_2 = 1$. In the picture, $(x,\ y,\ z)$ can move along the blue surface inside the gray area.

We first claim that f has a minimum at the boundaries i) or ii) depicted in Fig. A.1 For some constant c, consider a curve that appear as the intersection of two surfaces $(xz = k_2)$ and $(y - k_1 z = c)$. When $(x,\ y,\ z)$ moves along this curve, $f = x^2 + c^2$ decreases as x decreases. However, inside the gray area, the curve terminates at the boundaries i) or ii) whence x is minimized. Along the curve, therefore, f is minimized at the boundaries i) or ii). As every point $(x,\ y,\ z)$ lies on the curve for some choice of c, we conclude that the minimum of f arises at the boundaries i) or ii).

Now consider the minimization of f on the boundaries i) and ii) which are determined by the following equations:

$$\begin{aligned} &\text{i)}\ x^2 + y^2 = \frac{16}{\pi^2} \\ &\text{ii)}\ z = \frac{4}{\pi}. \end{aligned} \tag{A.3}$$

On the boundary i), f becomes

$$\begin{aligned} f &= x^2 + y^2 - 2k_1 yz + k_1^2 z^2 \\ &= \frac{16}{\pi^2} - 2k_1 yz + k_1^2 z^2. \end{aligned} \tag{A.4}$$

Using $(xz = k_2)$ and $(x^2 + y^2 = 16/\pi^2)$, we get

$$\frac{dz}{dy} = \frac{dz}{dx} \cdot \frac{dx}{dy} = \left(-\frac{z}{x}\right) \cdot \left(-\frac{y}{x}\right) = \frac{yz}{x^2} = \frac{k_2^2 y}{z}. \tag{A.5}$$

Differentiation of f with respect to y is

$$\begin{aligned} \frac{df}{dy} &= -2k_1 \left(z + y\frac{dz}{dy} - k_1 z \frac{dz}{dy} \right) \\ &= -2k_1 \left\{ \frac{k_2^2}{z} \left(y - \frac{k_1 z}{2} \right)^2 + \frac{z}{4}\left(4 - k_1^2 k_2^2\right) \right\} < 0. \end{aligned} \tag{A.6}$$

Hence, f decreases as y increases. This means that along the boundary i), f is minimized at the intersection of boundaries i) and ii).

Therefore, it suffices to consider the minimum of f on the boundary ii) only. Here, f becomes

$$f = k_2^2 \frac{\pi^2}{16} + \left(y - k_1 \frac{4}{\pi} \right)^2 \tag{A.7}$$

(A.7) is a quadratic function on y, where y takes its value in an interval

$$0 \le y \le \sqrt{\frac{16}{\pi^2} - \frac{k_2^2 \pi^2}{16}}. \tag{A.8}$$

If k_1 and k_2 satisfy

$$\frac{16k_1^2}{\pi^2} + \frac{k_2^2 \pi^2}{16} \le \frac{16}{\pi^2} \tag{A.9}$$

whence $4k_1/\pi$ lies in the interval, we know that f achieves the minimum at $y = 4k_1/\pi$ and the minimum value is

$$f\left(k_2 \frac{\pi}{4}, k_1 \frac{4}{\pi}, \frac{4}{\pi} \right) = k_2^2 \frac{\pi^2}{16}. \tag{A.10}$$

Otherwise, f takes the minimum at the intersection of boundaries i) and ii), namely

$$(x, y, z) = \left(k_2 \frac{\pi}{4}, \sqrt{\frac{16}{\pi^2} - k_2^2 \frac{\pi^2}{16}}, \frac{4}{\pi} \right). \tag{A.11}$$

In either case, f is minimized on $(z = 4/\pi)$.

Appendix B

The proposed method is implemented on the digital controller, TMS320C28335. The digital code is given in Table B.I for the implementation of the controller depicted in Fig. 4. The configuration and initialization codes including PWM, clock, sensing, and protection are not listed. The PWM gating is implemented using the ePWM module. A few important variables are Vo = sensed output voltage, Vref = reference voltage, Vc = control voltage, Vc_min, _max = minimum and maximum control voltages, and d1a and d1b = duty ratio signals in FCA domain.

Describing the code, a PI controller with an antiwindup produces the control voltage Vc from the error between the reference and the sensed voltage. The control voltage through a limiter is assigned to d1b while d1a is constant for fixed input and output voltages. The duty ratio signals are translated into the time-domain using the relationship in (21) using arcsine and arctangent functions. These trigonometric functions can be replaced by look-up table if reduced computational time is required. PWM gating is implemented by shifting phases of the

TABLE B.I
DIGITAL CODE FOR IMPLEMENTATION OF FDM

Function	Code
PI Controller	err_v = Vref − Vo; anti_v = err_v − kav∗(Vc − Vc2); intg_v + = kiv∗Ts∗anti_v; Vc = kpv∗err_v + intg_v;

Limiter	if(Vc < Vc_min) Vc2 = Vc_min;
	else if(Vc > Vc_max) Vc2 = Vc_max;
	else Vc2 = Vc;

Duty ratio assignment	d1b = Vc2; d1a = Vref/Vin_ref∗4/pi;

FCA to time-domain conversion	temp_a = pi/4∗sqrt(d1a∗d1a+d1b∗d1b);
	d1 = asin(temp_a)/pi;
	phi = atan(d1b/d1a)/2/pi;

PWM gating	phs1 = 0.5 − d1; phs2 = phi + 0.25 − 0.5∗d1; PHS1 = 2∗phs1∗PWM_half_period; PHS2 = 2∗phs2∗PWM_half_period; EPwm2Regs.TBPHS.half.TBPHS = PHS1; EPwm3Regs.TBPHS.half.TBPHS = PHS2; EPwm4Regs.TBPHS.half.TBPHS = PHS2;

TABLE B.II
DIGITAL CODE FOR IMPLEMENTATION OF PSM

Function	Code
PI Controller	err_v = Vref − Vo; anti_v = err_v − kav∗(Vc − Vc2); intg_v + = kiv∗Ts∗anti_v;

Limiter	Vc = kpv∗err_v + intg_v;
	if(Vc < Vc_min) Vc2 = Vc_min;
	else if(Vc > Vc_max) Vc2 = Vc_max;
	else Vc2 = Vc;

Phase assignment	phi = Vc2;
PWM gating	PHS1 = 2∗phi∗PWM_half_period; EPwm3Regs.TBPHS.half.TBPHS = PHS1; EPwm4Regs.TBPHS.half.TBPHS = PHS2;

PWMs of the bridges. PWM signals of switches in a leg are complementary to avoid arm short. Q_1 and Q_3 are controlled by ePWM1 with its phase fixed. ePWM2 is gating signal for Q_2 and Q_4. The secondary side is driven with full duty, $d_2 = 0.5$. Q_{5-8} are driven by ePWM3 and ePWM4 with which Q_5 and Q_6, and Q_7 and Q_8 are complementary pair, respectively.

The digital code for the implementation of PSM with a single voltage loop is delivered in Table B.II. Similarly, only the code of the voltage-loop controller is detailed, while excluding other configuration codes. PSM utilizes the phase as a single modulation variable. Gating signals for leg pairs within a bridge are equivalent

REFERENCES

[1] R. W. A. A. De Doncker, D. M. Divan, and M. H. Kheraluwala, "A three-phase soft-switched high-power-density dc/dc converter for high-power applications," *IEEE Trans. Ind. Appl.*, vol. 27, no. 1, pp. 63–73, Jan./Feb. 1991.

[2] B. Zhao, Q. Song, W. Liu, and Y. Sun, "Overview of dual-active-bridge isolated bidirectional dc–dc converter for high-frequency-link power-conversion system," *IEEE Trans. Power Electron.*, vol. 29, no. 8, pp. 4091–4106, Aug. 2014.

[3] T. Zhao, G. Wang, S. Bhattacharya, and A. Q. Huang, "Voltage and power balance control for a cascaded H-bridge converter-based solid-state transformer," *IEEE Trans. Power Electron.*, vol. 28, no. 4, pp. 1523–1532, Apr. 2013.

[4] H. Fan and H. Li, "High-frequency transformer isolated bidirectional dc–dc converter modules with high efficiency over wide load range for 20 kVA solid-state transformer," *IEEE Trans. Power Electron.*, vol. 26, no. 12, pp. 3599–3608, Dec. 2011.

[5] J. E. Huber and J. W. Kolar, "Volume/weight/cost comparison of a 1MVA 10 kV/400 V solid-state against a conventional low-frequency distribution transformer," in *Proc. IEEE Energy Convers. Congr. Expo.*, 2014, pp. 4545–4552.

[6] D. Dujic, F. Kieferndorf, F. Canales, and U. Drofenik, "Power electronic traction transformer technology," in *Proc. IEEE Power Electron. Motion Control Conf.*, 2012, pp. 636–642.

[7] N. Soltau, H. Stagge, R. W. De Doncker, and O. Apeldoorn, "Development and demonstration of a medium-voltage high-power DC-DC converter for DC distribution systems," in *Proc. IEEE Power Electron. Distrib. Gener. Syst. Conf.*, 2014, pp. 1–8.

[8] S. Inoue and H. Akagi, "A bi-directional isolated dc/dc converter as a core circuit of the next-generation medium-voltage power conversion system," in *Proc. IEEE Power Electron. Spec. Conf.* 2006, pp. 1–7.

[9] H. Qin and J. W. Kimball, "Generalized average modeling of dual active bridge dc–dc converter," *IEEE Trans. Power Electron.*, vol. 27, no. 4, pp. 2078–2084, Apr. 2012.

[10] X. Li and Y. Li, "An optimized phase-shift modulation for fast transient response in a dual-active-bridge converter," *IEEE Trans. Power Electron.*, vol. 29, no. 6, pp. 2661–2665, Jun. 2014.

[11] N. Schibli, "Symmetrical multilevel converters with two quadrant dc-dc feeding," Ph.D. dissertation, Faculty of Eng. Science and Technology, Ecole Polytech. Federale de Lausanne, Lausanne, Switzerland, 2000.

[12] F. Krismer, S. Round, and J. W. Kolar, "Performance optimization of a high current dual active bridge with a wide operating voltage range," in *Proc. IEEE Power Electron. Spec. Conf.*, 2006, pp. 1–7.

[13] H. Zhou and A. M. Khambadkone, "Hybrid modulation for dual-active-bridge bidirectional converter with extended power range for ultracapacitor application," *IEEE Trans. Ind. Appl.*, vol. 45, no. 4, pp. 1434–1442, Jul./Aug. 2009.

[14] F. Jauch and J. Biela, "Generalized modeling and optimization of a bidirectional dual active bridge dc-dc converter including frequency variation," in *Proc. IEEE Power Electron. Conf.*, 2014, pp. 1788–1795.

[15] H. Bai and C. Mi, "Eliminate reactive power and increase system efficiency of isolated bidirectional dual-active-bridge dc–dc converters using novel dual-phase-shift control," *IEEE Trans. Power Electron.*, vol. 23, no. 6, pp. 2905–2914, Nov. 2008.

[16] B. Zhao, Q. Song, and W. Liu, "Efficiency characterization and optimization of isolated bidirectional dc–dc converter based on dual-phase-shift control for dc distribution application," *IEEE Trans. Power Electron.*, vol. 28, no. 4, pp. 1711–1727, Apr. 2013.

[17] H. Wen, W. Xiao, and B. Su, "Nonactive power loss minimization in a bidirectional isolated dc–dc converter for distributed power systems," *IEEE Trans. Ind. Electron.*, vol. 61, no. 12, pp. 6822–6831, Dec. 2014.

[18] J. Huang, Y. Wang, Y. Gao, W. Lei, and N. Li, "Modified unified PWM control to operate the dual active bridge converters under ZVS in the whole load range," in *Proc. IEEE ECCE Asia Conf.*, 2013, pp. 620–625.

[19] X. F. He, Z. Zhang, Y. Y. Cai, and Y. F. Liu, "A variable switching frequency hybrid control for ZVS dual active bridge converters to achieve high efficiency in wide load range," in *Proc. IEEE Appl. Power Electron. Conf.*, 2014, pp. 1095–1099.

[20] J. Everts, F. Krismer, J. Van den Keybus, J. Driesen, and J. W. Kolar, "Optimal ZVS modulation of single-phase single-stage bidirectional DAB ac–dc converters," *IEEE Trans. Power Electron.*, vol. 29, no. 8, pp. 3954–3970, Aug. 2014.

[21] F. Krismer and J. W. Kolar, "Efficiency-optimized high-current dual active bridge converter for automotive applications," *IEEE Trans. Ind. Electron.*, vol. 59, no. 7, pp. 2745–2760, Jul. 2012.

[22] F. Krismer and J. W. Kolar, "Closed form solution for minimum conduction loss modulation of DAB converters," *IEEE Trans. Power Electron.*, vol. 27, no. 1, pp. 174–188, Jan. 2012.

[23] A. K. Jain and R. Ayyanar, "PWM control of dual active bridge: Comprehensive analysis and experimental verification," *IEEE Trans. Power Electron.*, vol. 26, no. 4, pp. 1215–1227, Apr. 2011.

[24] B. Zhao, Q. Song, W. Liu, G. Liu, and Y. Zhao, "Universal high-frequency-link characterization and practical fundamental-optimal strategy for

dual-active-bridge dc-dc converter under PWM plus phase-shift control," *IEEE Trans. Power Electron.*, vol. 30, no. 12, pp. 6488–6494, Dec. 2015.
[25] J. Itoh, H. Higa, and T. Nagano, "A novel control method focusing on reactive power for a dual active bridge converter," in *Proc. IEEE Electron. Appl. Conf. Expo.*, 2014, pp. 1020–1025.
[26] F. Krismer and J. W. Kolar, "Accurate power loss model derivation of a high-current dual active bridge converter for an automotive application," *IEEE Trans. Ind. Electron.*, vol. 57, no. 3, pp. 881–891, Mar. 2010.
[27] Y. Jang, M. M. Jovanovic, and Y. Chang, "A new ZVS-PWM full-bridge converter," *IEEE Trans. Power Electron.*, vol. 18, no. 5, pp. 1122–1129, Sep. 2003.

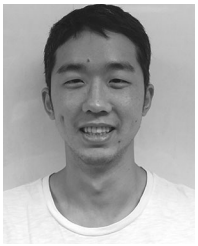

Wooin Choi (S'12) received the B.S. and M.S. degrees in electrical engineering from Seoul National University, Seoul, Korea, in 2011 and 2013, respectively, where he is currently working toward the Ph.D. degree.

His current research interests include power electronics, dc–dc conversion, and design and control of dc microgrid.

Kyung-Min Rho received the B.S. degree majoring in mathematics and minoring in electrical engineering from Seoul National University, Seoul, Korea, in 2014, where he is currently working toward the Master's degree majoring in mathematics.

His current research interests include algebraic topology, symplectic geometry, and mirror symmetry.

Bo-Hyung Cho (M'89–SM'95–F'11) received the B.S. and M.S. degrees from the California Institute of Technology, Pasadena, CA, USA, in 1975 and 1980, respectively, and the Ph.D. degree from Virginia Polytechnic Institute and State University (Virginia Tech), Blacksburg, VA, USA, in 1985, all in electrical engineering.

Prior to his research with Virginia Tech, he was a Member of the Technical Staff with the Department of Power Conversion Electronics, TRW Defense and Space System Group. From 1982 to 1995, he was a Professor with the Department of Electrical Engineering, Virginia Tech. In 1995, he joined the School of Electrical Engineering, Seoul National University, Seoul, Korea, where he is currently a Professor. His current research interests include power electronics, modeling, analysis, and control of spacecraft power processing equipment, and distributed power systems.

Dr. Cho is a Member of the Tau Beta Pi. He received the 1989 Presidential Young Investigator Award from the National Science Foundation. He chaired the 2006 *IEEE Power Electronics Specialists Conference*.